



Originally published as:

Gavryushkin, P. N., Bekhtenova, A., Lobanov, S. S., Shatskiy, A., Likhacheva, A. Y., Sagatova, D., Sagatov, N., Rashchenko, S. V., Litasov, K. D., Sharygin, I. S., Goncharov, A. F., Prakapenka, V. B., Higo, Y. (2019): High-Pressure Phase Diagrams of Na₂CO₃ and K₂CO₃. - *Minerals*, 9, 10.

DOI: <http://doi.org/10.3390/min9100599>

Article

High-Pressure Phase Diagrams of Na_2CO_3 and K_2CO_3

Pavel N. Gavryushkin ^{1,2,*}, Altyna Bekhtenova ^{1,2}, Sergey S. Lobanov ³, Anton Shatskiy ^{1,2}, Anna Yu. Likhacheva ^{2,4}, Dinara Sagatova ^{1,2}, Nursultan Sagatov ^{1,2}, Sergey V. Rashchenko ^{1,2,4}, Konstantin D. Litasov ^{1,2}, Igor S. Sharygin ^{5,6}, Alexander F. Goncharov ⁷, Vitali B. Prakapenka ⁸ and Yuji Higo ⁹

¹ Department of Geology and Geophysics, Novosibirsk State University, Pirogova 2, 630090 Novosibirsk, Russia; bekhtenova@igm.nsc.ru (A.B.); anton.antonshatskiy.shatskiy@gmail.com (A.S.); d.sagatova1729@gmail.com (D.S.); sagatinho23@gmail.com (N.S.); rashchenko@igm.nsc.ru (S.V.R.); klitasov@igm.nsc.ru (K.D.L.)

² Sobolev Institute of Geology and Mineralogy, Siberian Branch of the Russian Academy of Science, prosp. acad. Koptyuga 3, 630090 Novosibirsk, Russia; alih@igm.nsc.ru

³ GFZ German Research Center for Geosciences, Section 4.3, Telegrafenberg, 14473 Potsdam, Germany; slobanov@gfz-potsdam.de

⁴ Budker Institute of Nuclear Physics, Siberian Branch of the Russian Academy of Science, pr. ac. Lavrentieva 11, 630090 Novosibirsk, Russia

⁵ Center for Northeast Asian Studies, Tohoku University, 41 Kawauchi, Aoba-ku, Sendai, Miyagi 980-8576, Japan; igor.sharygin@gmail.com

⁶ Institute of the Earth's Crust, Siberian Branch of the Russian Academy of Science, Lermontov Street 128, Irkutsk 664033, Russia

⁷ Geophysical Laboratory, Carnegie Institution of Washington, Washington, DC 20015, USA; agoncharov@carnegiescience.edu

⁸ Center for Advanced Radiation Sources, University of Chicago, Chicago, IN 60637, USA; prakapenka@cars.uchicago.edu

⁹ Japan Synchrotron Radiation Research Institute, SPring-8, Kouto, Hyogo 678-5198, Japan; higo@spring8.or.jp

* Correspondence: gavryushkin@igm.nsc.ru or p.gavryushkin@g.nsu.ru

Received: 16 August 2019; Accepted: 26 September 2019; Published: 30 September 2019



Abstract: The phase diagrams of Na_2CO_3 and K_2CO_3 have been determined with multianvil (MA) and diamond anvil cell (DAC) techniques. In MA experiments with heating, $\gamma\text{-Na}_2\text{CO}_3$ is stable up to 12 GPa and above this pressure transforms to $P6_3/mcm$ -phase. At 26 GPa, $\text{Na}_2\text{CO}_3\text{-}P6_3/mcm$ transforms to the new phase with a diffraction pattern similar to that of the theoretically predicted $\text{Na}_2\text{CO}_3\text{-}P2_1/m$. On cold compression in DAC experiments, $\gamma\text{-Na}_2\text{CO}_3$ is stable up to the maximum pressure reached of 25 GPa. K_2CO_3 shows a more complex sequence of phase transitions. Unlike $\gamma\text{-Na}_2\text{CO}_3$, $\gamma\text{-K}_2\text{CO}_3$ has a narrow stability field. At 3 GPa, K_2CO_3 presents in the form of the new phase, called $\text{K}_2\text{CO}_3\text{-III}$, which transforms into another new phase, $\text{K}_2\text{CO}_3\text{-IV}$, above 9 GPa. In the pressure range of 9–15 GPa, another new phase or the mixture of phases III and IV is observed. The diffraction pattern of $\text{K}_2\text{CO}_3\text{-IV}$ has similarities with that of the theoretically predicted $\text{K}_2\text{CO}_3\text{-}P2_1/m$ and most of the diffraction peaks can be indexed with this structure. Water has a dramatic effect on the phase transitions of K_2CO_3 . Reconstruction of the diffraction pattern of $\gamma\text{-K}_2\text{CO}_3$ is observed at pressures of 0.5–3.1 GPa if the DAC is loaded on the air.

Keywords: carbonate; diamond anvil cell; multi anvil apparatus; laser heating; resistive heating; global carbon cycle; indexing; density functional theory

1. Introduction

Natural occurrence of alkaline carbonates Na_2CO_3 and K_2CO_3 is in the form of rare minerals natrite Na_2CO_3 [1] and gregoryite $(\text{Na}_2, \text{K}_2, \text{Ca})\text{CO}_3$ [2,3] and as a constituent part of double carbonates: Nyerereite and zemkorite $(\text{Na}, \text{K})_2\text{Ca}(\text{CO}_3)_2$ [4–8], shortite $\text{Na}_2\text{Ca}_2(\text{CO}_3)_3$ [9], eitelite $\text{Na}_2\text{Mg}(\text{CO}_3)_2$ [10] and polymorphs of $\text{K}_2\text{Ca}(\text{CO}_3)_2$ butchelite and fairchildite [11]. Other than these minerals, a number of double Na–Ca, Na–Fe and K–Mg carbonates were synthesised experimentally at pressures up to 6 GPa: $\text{Na}_2\text{Ca}_3(\text{CO}_3)_4$, $\text{Na}_2\text{Ca}_4(\text{CO}_3)_5$, $\text{Na}_4\text{Ca}(\text{CO}_3)_3$, $\text{Na}_6\text{Ca}_5(\text{CO}_3)_8$, Na_2FeCO_3 , $\text{K}_2\text{Mg}(\text{CO}_3)_2$ [12–20].

Despite a relatively small number of findings of simple alkaline and double alkaline–alkaline-earth carbonates, gregoryite together with nyerereite form the main part of unique natrocarbonatites rocks of the Oldoinyo-Lengai volcano (Tanzania) [6]. Nahcolite (NaHCO_3), eitelite and nyerereite were also found in carbonatitic inclusions in diamonds from the Juina, Mato Grosso State, Brazil [21,22]. The summary of other findings of double alkaline–alkaline-earth carbonates can be found elsewhere [5]. All these findings gave rise to intensive experimental investigation of Na_2CO_3 and K_2CO_3 melting curves in the pressure range of the upper mantle and transition zone of the Earth [19,23–29]. The melting curve of Na_2CO_3 was found to be smooth in the range of 3–18 GPa [23], while on the melting curve of K_2CO_3 , two kinks, at 5 and 9 GPa, have been found at 2–20 GPa [24,25]. High-pressure transitions in solid phases of Na_2CO_3 and K_2CO_3 have been investigated only in one work, published as a PhD thesis [24]. In this work, three high pressure phases of K_2CO_3 , *new phase 1*, *new phase 2* and *new phase 3* have been revealed. Crystal structures of these phases have not been determined and are still unknown.

Theoretically, phase transitions of alkaline carbonates have been investigated by Čančarevič and co-authors [30] and in our recent work [31]. Here, we report the results of in situ X-ray diffraction experiments with both multianvil (MA) and diamond anvil cell (DAC) techniques on the determination of Na_2CO_3 and K_2CO_3 P–T phase diagrams and the results of the indexing of high-pressure diffraction patterns with theoretically predicted structures.

2. Methods

2.1. Experimental Techniques

The high-pressure high-temperature behaviour of K_2CO_3 and Na_2CO_3 have been investigated with in situ X-ray diffraction experiments. For both compounds, large volume multianvil apparatus and DAC experiments have been performed. DAC experiments were of three different types: (1) Na_2CO_3 , without heating and pressures up to 25 GPa, performed at Advanced Photon Source (APS); (2) K_2CO_3 , with laser heating and pressures up to 50 GPa, also performed at APS; (3) K_2CO_3 , without heating and pressures in the range of 0.5–7 GPa, at the Siberian Synchrotron and Terahertz Radiation Centre (SSTRC). The first two types of experiments we will designate as DAC-APS and the last one as DAC-SSTRC.

Synthetic reagents of K_2CO_3 and Na_2CO_3 produced by Wako Co Ltd. (Wakayama, Japan) (99.99%, MA and DAC-SSTRC experiments) and Fischer Scientific (Pittsburgh, PA, USA) (>99.5%, DAC-APS experiments) have been used as the starting materials.

2.1.1 MA Experiments

The in situ X-ray diffraction experiments M964, M965, M967 and M1128 were conducted at the Spring-8 synchrotron radiation facility (Hyogo Prefecture, Japan), using a Kawai-type high-pressure apparatus, “SPEED-MkII”, installed at a bending magnet beam line BL04B1 [32]. An energy-dispersive X-ray diffraction technique was used for the in situ measurements. The incident X-rays were collimated to form a thin beam with dimensions of 0.05 mm in the horizontal direction and 0.1 mm in the vertical direction by tungsten carbide slits and directed to the sample through a pyrophyllite gasket and X-ray windows in the cell. A Ge solid-state detector with a 4096-channel analyzer was used, which was calibrated by using characteristic X-rays of Cu, Mo, Ag, La, Ta, Pt, Au and Pb. The diffraction angle (2θ)

was approximately 5.5° , calibrated before compression, using the known d -values of X-ray diffraction peaks of Au (note volumes used in the beam line software: $V_0 = 67.847 \text{ \AA}^3$), with an uncertainty of less than 0.0005° . In order to obtain diffraction patterns with a reasonable number of lines, a special oscillation system to rotate the press from -3° to $+6^\circ$ has been employed [32]. We used ultra-hard 26 mm WC anvils ("Fujillo," TF-05) with a truncated edge length of 2.0 mm to compress a Co-doped MgO pressure medium shaped in form of octahedron with grinded edges and corners with edge length of 6.2 mm. Pyrophyllite gaskets with 2.0 mm thickness and 3.4 mm width were used to support anvil flanks. A TiB_2 tubular heater, 1.7/1.1 mm in outer/inner diameter and 2.0 mm length was employed to heat the sample. $\text{WRe}_{3\%/25\%}$ thermocouple, 0.05 mm in diameter, with junction placed just above the sample capsule was used to control temperature. To avoid thermocouple cut during compression, thicker thermocouple wires (0.15 + 0.10 mm) were inserted through the gaskets into the pressure medium. The sample, reagent grade Na_2CO_3 or K_2CO_3 powder, was blended with Au powder in 10:1 weight ratio in an agate mortar under acetone. The powder was compressed to a cylinder, 0.5 mm in height and 0.9 mm in diameter and then dried at 300°C for two hours. The sample was loaded into a h-BN capsule with wall thickness of 0.15 mm. The materials with low X-ray absorption were placed on the way of X-ray beam, namely, MgO cylinders, 1.0 mm in diameter and 0.5 mm in thickness were inserted from outside and a 5- μm diamond powder was loaded into the hole 0.7 mm in diameter and 1.0 mm in length inside.

The cell assembly was first compressed to nearly the maximum press load at ambient temperature. Thereafter, we followed a complex P-T-path with several heating cycles while continuously taking diffraction patterns. Exposure times for collecting diffraction data were 200 s. The experimental pressures at high temperatures were calculated from the unit cell volume of Au using the equation of state reported in [33] with <0.05 GPa deviation. Typically, 4 of the diffraction lines (111), (200), (220) and (311) of Au were used to calculate the pressure and 7–10 major diffraction lines were used to calculate the volume of Na_2CO_3 .

2.1.2 DAC-APS

In DAC-APS experiments we used symmetric DACs equipped with 300 μm brilliant-cut diamonds. Rhenium gaskets were preindented to a thickness of $\sim 40 \mu\text{m}$ and laser-cut in the center of the indentation in order to create a sample chamber of $\sim 100 \mu\text{m}$ in diameter. To prevent sample contamination with water, Na_2CO_3 or K_2CO_3 reagents were annealed at 250°C for 30 h, sealed and transported to an Ar glovebox for DAC loadings. Upon sample loading, the minute amount of Pt/Au powder was mixed into the $\text{K}_2\text{CO}_3/\text{Na}_2\text{CO}_3$ samples. Neon was gas-loaded as a pressure medium at 0.2 GPa.

Compression runs were performed at the 13ID-D undulator beamline of GeoSoilEnviroCARS, Advanced Photon Source, Argonne National Laboratory. The X-ray beam ($\lambda = 0.3344 \text{ \AA}$) was focused to a $\sim 3 \times 5 \mu\text{m}$ spot size. High temperatures (up to 2600 K) were achieved through double-sided Nd:YLF laser-heating system with a 20 μm diameter focused laser beam [34] coupled to Pt powder. Temperature was measured by spectroradiometry simultaneously with XRD measurements. Collected spectra were fit to blackbody radiation function using T-Rax software (developed by C. Prescher). The uncertainty in temperature measurement is assumed to be typical of laser-heated DACs (~ 150 K). Overall heating duration was about 10–20 min. After quenching, the samples were mapped with the X-ray. Every sample was heated in at least two areas.

2.1.3 DAC-SSTRC

Three different experiments have been performed as SSTRC: (1) With silicon oil as pressure transmitting medium and loading in a glovebox; (2) with silicon oil and loading on the air; (3) with methanol as a pressure transmitting medium and also loading on the air. The results of experiment (2) have been published in [35] and here we use them only for comparison.

Sample of K_2CO_3 was preliminarily annealed in a vacuum oven at 200 °C for 2 h, then ground in an agate mortar and mixed with pressure transmitting medium in a ratio of 1:4. This mixture was loaded in a 400 μm hole in a stainless steel gasket of 100 μm thickness under ambient conditions or in an Ar glovebox. Mao-Bell DACs were used to generate pressures up to 7 GPa.

In situ X-ray diffraction experiments were conducted at the beamline #4 of the VEPP-3 storage ring of the SSTRC (Novosibirsk, Russia) ($\lambda = 0.3685 \text{ \AA}$) [36]. MAR345 imaging plate detector (pixel dimension 100 μm) was used for data collecting. FIT2D [37] program was used to integrate the two-dimensional images to a maximum 2θ value of 25°. The pressure was measured by displacement of $^5D_0 - ^7F_0$ fluorescence line of $\text{SrB}_4\text{O}_7:\text{Sm}^{2+}$ [38] with PRL (BETSA) spectrometer with accuracy of ~ 0.05 GPa.

2.2. Details of Ab Initio Calculations

For indexing of experimental diffraction patterns, structural models of $\gamma\text{-Na}_2\text{CO}_3$, $\text{Na}_2\text{CO}_3\text{-}P6_3/mcm$, $\text{Na}_2\text{CO}_3\text{-}P2_1/m$, $\gamma\text{-K}_2\text{CO}_3$ and $\text{K}_2\text{CO}_3\text{-}P\bar{1}$ [31] were optimised with density functional theory (DFT). Incommensurate modulations of $\gamma\text{-Na}_2\text{CO}_3$ structure [39] have not been considered. Optimisations have been performed using the plane wave basis set and the projector augmented wave method [40], as implemented in VASP code [41–43]. Exchange-correlation effects were taken into account within LDA (local density approximation) and GGA (generalised gradient approximation) with Perdew–Burke–Ernzerhof functional [44]. LDA pseudopotentials with $3s^23p^64s^1, 2p^63s^1, 2s^22p^4$ and $2s^22p^2$ valence electrons and GGA pseudopotentials with $3s^23p^64s^13d^0, 3s^13p^0, 2s^22p^4$ and $2s^22p^2$ electrons have been used for K, Na, O and C, respectively. A plane-wave basis set cutoff energy were set to 520 eV. The Brillouin zone was sampled using uniform Γ -centred k-point meshes with a k-point grid of $2\pi \times 0.025 \text{ \AA}^{-1}$ spacing. The iterative relaxation of atomic positions was stopped when all forces acting on atoms were smaller than $0.001 \text{ eV \AA}^{-1}$. After optimisation, symmetry of the structures were analysed with FINDSYM program [45]. VESTA software [46] have been used for the structure visualisation.

To take into account the temperature effect and calculate monovariant boundaries on P-T diagrams, we used the method of lattice dynamics within the quasi-harmonic approximation (QHA). The phonon frequencies and phonon dispersion curves were calculated with the PHONOPY 2.3 package [47]. The energy cut-off in this case was increased to 800 eV. Real-space force constants were calculated using supercell method and finite difference method as implemented in PHONOPY, with a $2 \times 2 \times 2$ supercell for $\text{Na}_2\text{CO}_3\text{-}Pm\bar{m}n$, $\text{Na}_2\text{CO}_3\text{-}P6_3/mcm$, $\text{Na}_2\text{CO}_3\text{-}P2_1/m$, $\text{K}_2\text{CO}_3\text{-}P2_1/m$, $\text{K}_2\text{CO}_3\text{-}C2/c$, $\beta\text{-K}_2\text{CO}_3$, a $1 \times 2 \times 2$ supercell for $\gamma\text{-Na}_2\text{CO}_3$ and a $2 \times 1 \times 2$ supercell for $\gamma\text{-K}_2\text{CO}_3$. Helmholtz free energies were computed for all structures at seven volumes starting from 0 GPa to 60 GPa, then corrected for thermal expansion using the quasiharmonic approximation.

2.3. Indexing

For unbiased comparison of diffraction patterns with that of theoretical structures, we used cell parameters directly from DFT calculations without any refinement. In the case of unambiguous correspondence, Pawley and Rietveld refinements have been performed. As LDA pseudopotential slightly underestimates, whereas GGA overestimates unit cell volume, we used structures with cell parameters averaged between LDA and GGA optimisations. As we will show below, such a simple technique gives the cell parameters that sufficiently better reproduce experimental values than LDA or GGA optimisations.

The phase identification and preliminary analysis of all the diffraction patterns have been performed with “PDIndexer” software [48]. For analysis of diffraction patterns recorded at Spring8 “XRyAnalysis” software, provided by the beamline, have been also used. Pawley and Rietveld refinements were performed with GSAS-II software [49]. The uncertainties in the unit cell volume of Au, determined by a least-squares fit, give typically less than 0.1 GPa uncertainty in pressure.

3. Results And Discussion

3.1. Na_2CO_3

In MA experiments, $\gamma\text{-Na}_2\text{CO}_3$ is stable from 1 atm to 12 GPa and then two phase transitions at 12 GPa and at 26 GPa take place, see Figure 1a. In room temperature DAC-APS experiments, substantial changes in $\gamma\text{-Na}_2\text{CO}_3$ diffraction patterns are not observed up to the maximum reached pressure of 25 GPa (Figure 1). Splitting of (401) diffraction peak, marked on Figure 1b with a star, can be explained by the increasing of intensities of (400) and (200) reflections of $\gamma\text{-Na}_2\text{CO}_3$ or by the some structural changes of $\gamma\text{-Na}_2\text{CO}_3$.

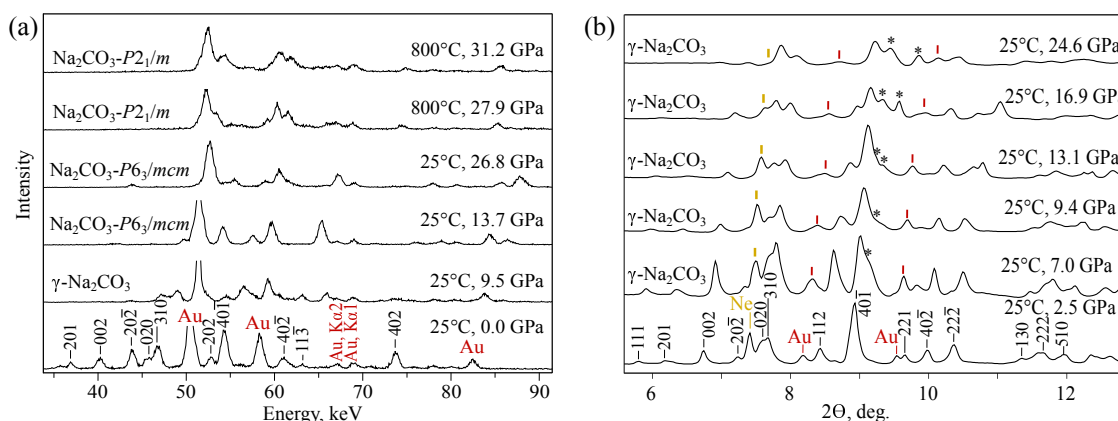


Figure 1. Diffraction patterns of Na_2CO_3 obtained in MA (a) and DAC (b) experiments.

The pressures of phase transitions in MA experiments are consistent with theoretical predictions [31]. According to calculations [31], Na_2CO_3 undergoes two phase transitions in the pressure range of 0–40 GPa, first at 5 GPa from γ - to $P6_3/mcm$ -phase and another at 35 GPa, from $P6_3/mcm$ - to $P2_1/m$ -phase.

As can be seen from Figure 2a,c theoretical diffraction peaks of γ - and $P6_3/mcm$ -structures exactly reproduce experimental ones. The Pawley fit has been performed with the following R-factors (Figure 2b,d): $\gamma\text{-Na}_2\text{CO}_3$: R-bkg = 7.54%, wR-bkg = 13.49%, $P6_3/mcm$: R-bkg = 10.80%, wR-bkg = 19.95%. The difference between cell parameters before and after refinement does not exceed 0.07 Å for γ and 0.03 Å for $P6_3/mcm$ structures. For the LDA and GGA optimised $P6_3/mcm$ structure (without averaging) these deviations are sufficiently higher and reach 0.92 Å and 0.71 Å, respectively. This illustrates the efficiency of the technique when the structure averaged between LDA and GGA optimisations is used for the indexing (Figure S1). For a $P6_3/mcm$ structure, the Rietveld refinement has also been performed, see Figure S2. It also confirms the consistency of the $P6_3/mcm$ structure with the obtained diffraction pattern.

Indexing of diffraction patterns, recorded above 27 GPa, with $P2_1/m$ structure are ambiguous (Figure 3). The quality and number of diffraction peaks is not enough to perform the reliable Pawley fit. However, most of the experimental peaks can be indexed with $P2_1/m$ structure (Figure 3). Based on this we consider $P2_1/m$ structure as the structure of high-pressure polymorph of Na_2CO_3 observed above 26 GPa.

The obtained P-T diagram (Figure 4) is consistent with available experimental data on the melting curve of Na_2CO_3 . According to these data, the melting temperature of Na_2CO_3 is 1980 K at 17 GPa and up to this pressure the melting curve has no kinks [23]. Extrapolation of the phase boundary between γ - and $P6_3/mcm$ phases (Figure 4) to the melting temperatures shows, the first kink on the melting curve appears at 18–19 GPa. This is consistent with the smooth character of the melting curve up to 17 GPa observed in the experiment [23].

In our previous work [50], we suggested the transition from $\gamma\text{-Na}_2\text{CO}_3$ to $\beta\text{-Na}_2\text{CO}_3$ at 1–2 GPa. Both phases have similar structures, complicated by the incommensurate modulations in the case of

γ - Na_2CO_3 [39]. Distinguishing these two phases in our MA energy-dispersive diffraction patterns is problematic and here we designate both of them as γ - Na_2CO_3 , assuming that this can be γ - or β -phase.

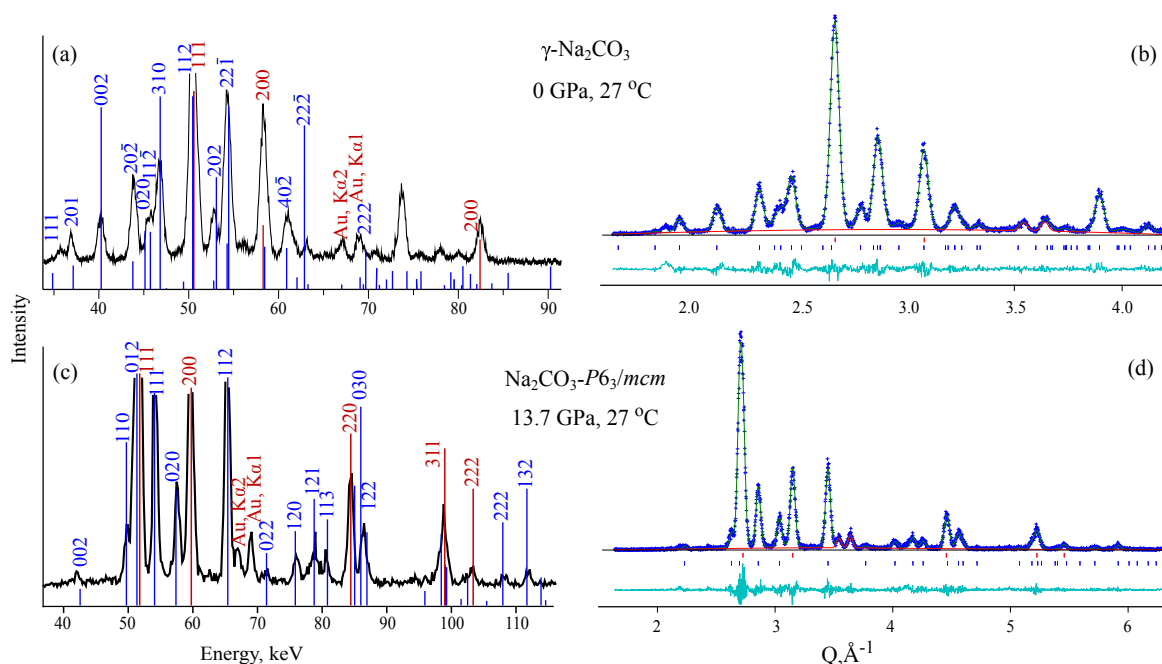


Figure 2. Indexing of diffraction patterns with γ - (a) and $P6_3/mcm$ (c) structures of Na_2CO_3 and corresponding Pawley refinements (b,d). Blue bars correspond to the theoretical peaks of γ - Na_2CO_3 (a,b) and Na_2CO_3 - $P6_3/mcm$, red bars to the peaks of Au.

The unit cell parameters and atomic coordinates of $P6_3/mcm$ - and $P2_1/m$ -phases are shown in Table 1, dependencies of the cell parameters on pressure for γ - and $P6_3/mcm$ determined in MA experiments—in Table 2 and for γ -phase determined in DAC experiments—in Table S1. The difference in $V(P)$ dependencies for γ -phase determined in DAC and MA experiments at pressures above 10 GPa (Figure 5) can be explained by the transition to the metastable phase with similar structure, taking place on cold compression in DAC. This hypothesis is consistent with the changing of peak intensities and the appearance of the new peaks in the DAC experiment (Figure 1b). A similar situation is observed for CaCO_3 . On cold compression of calcite (CaCO_3) it transforms to the number of metastable structures CaCO_3 -II, III, IIIb, VI [51], none of which is observed in experiments with heating and only transition to the stable modification, aragonite, takes place ([52,53]).

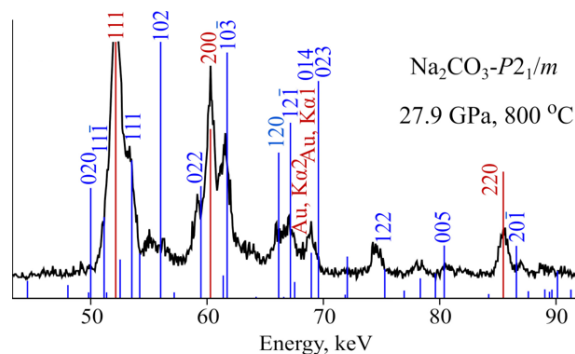


Figure 3. Indexing of experimental diffraction pattern recorded at 27.9 GPa with $P2_1/m$ structure of Na_2CO_3 .

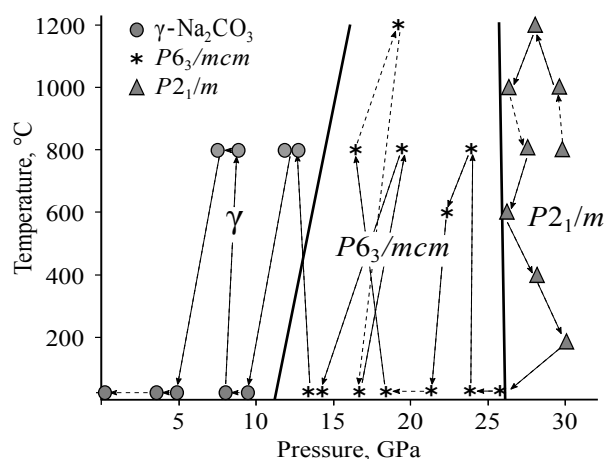


Figure 4. Phase diagram of Na_2CO_3 according to MA experiments.

Table 1. Structural data for high-pressure phases of Na_2CO_3 used for indexing and refinements. Cell parameters of $P6_3/mcm$ - and γ phases according to Pawley refinement, other structural data according to DFT calculations.

Pr.,Temp. (GPa, °C)	Space Group	Lattice Parameters Å, deg.			Atomic Coordinates			
					Species	x	y	z
$\gamma\text{-Na}_2\text{CO}_3$								
1 atm, 25	$C2/m$	$a = 8.90(2)$	$b = 5.26(2)$	$c = 6.04(3)$	Na1	0.00	0.00	0.00
		$\alpha = 90$	$\beta = 101.29(7)$	$\gamma = 90$	Na2	0.00	0.00	0.50
					Na3	0.17	0.16	0.74
					C1	0.16	0.17	0.25
					O1	0.10	0.10	0.28
					O2	0.29	0.10	0.18
$\text{Na}_2\text{CO}_3\text{-}P6_3/mcm$								
13.7, 25	$P6_3/mcm$	$a = 4.776(1)$	$b = 4.776(1)$	$c = 5.630(1)$	Na1	0.33	0.67	0.00
		$\alpha = 90$	$\beta = 90$	$\gamma = 120$	C1	0.00	0.00	0.25
					O1	0.73	0.00	0.25
$\text{Na}_2\text{CO}_3\text{-}C2/m$								
27.9, 800	$P2_1/m$	$a = 2.77$	$b = 4.75$	$c = 7.44$	Na1	0.63	0.25	0.37
		$\alpha = 90$	$\beta = 97.47$	$\gamma = 90$	Na2	0.52	0.25	0.03
					C1	0.01	0.25	0.73
					O1	0.07	0.52	0.19
					O2	0.20	0.25	0.59

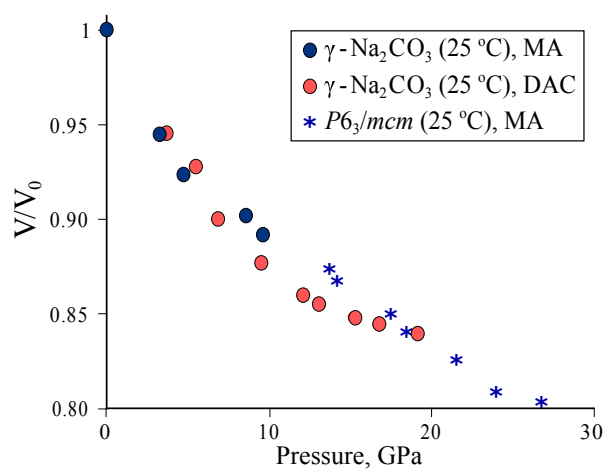


Figure 5. The dependencies of volume on pressure for γ - and $P6_3/mcm$ phases of Na_2CO_3 , determined in MA and DAC experiments at room temperature.

Table 2. Unit cell parameters of γ - and $P6_3/mcm$ -phases of Na_2CO_3 according to MA experiments.

Pressure (GPa)	Temperature ($^{\circ}\text{C}$)	Unit Cell Parameters (\AA , deg.)				Volume (\AA^3)
		<i>a</i>	<i>b</i>	<i>c</i>	β	
$\gamma\text{-Na}_2\text{CO}_3$						
0.0	25	8.89(5)	5.27(2)	6.05(3)	101.33(7)	277.7(31)
3.3	25	8.73(5)	5.16(2)	5.95(3)	101.54(7)	262.7(31)
4.7	25	8.69(5)	5.12(2)	5.89(3)	101.65(7)	256.8(31)
8.6	25	8.55(5)	5.07(2)	5.91(3)	101.44(7)	250.9(31)
9.6	25	8.53(5)	5.06(2)	5.86(3)	101.67(7)	248.0(31)
7.4	800	8.70(5)	5.13(2)	5.91(3)	101.16(7)	259.0(31)
8.8	800	8.65(5)	5.13(2)	5.90(3)	101.41(7)	256.5(31)
12.0	800	8.55(5)	5.06(2)	5.93(3)	101.04(7)	251.5(31)
13.0	800	8.53(5)	5.06(2)	5.90(3)	101.53(7)	249.5(31)
$P6_3/mcm\text{-Na}_2\text{CO}_3$						
13.7	25	4.783(2)	4.783(2)	5.621(1)		111.11(7)
14.2	25	4.775(2)	4.775(2)	5.597(1)		110.22(7)
17.5	25	4.742(2)	4.742(2)	5.562(1)		108.11(7)
18.5	25	4.726(2)	4.726(2)	5.544(1)		106.81(7)
21.5	25	4.691(2)	4.691(2)	5.503(1)		104.90(7)
24.0	25	4.670(2)	4.670(2)	5.451(1)		102.81(7)
26.8	25	4.668(2)	4.668(2)	5.436(1)		102.02(7)
15.4	800	4.784(2)	4.748(2)	5.658(1)		111.71(7)
20.4	800	4.731(2)	4.731(2)	5.583(1)		108.07(7)

3.2. K_2CO_3

3.2.1 MA and DAC-APS Results

Both DAC and MA experiments show consistent results on phase transitions of K_2CO_3 . The same phase transitions are observed in both experiments and differences in pressures of the transitions do not exceed 3 GPa. Below we give pressures of phase transitions according to the MA experiment.

In both DAC-APS and MA experiments three high-pressure phase transitions are observed (Figure 6); the first takes place at less than 3 GPa, the second-at 10 and the third-at 15 GPa. The phase stable below 3 GPa, in the range of 3–10 GPa and above 15 GPa we will designate as $\text{K}_2\text{CO}_3\text{-II}$, $\text{K}_2\text{CO}_3\text{-III}$ and $\text{K}_2\text{CO}_3\text{-IV}$, respectively. The existence of the phase $\text{K}_2\text{CO}_3\text{-II}$ is assumed based on the experimental data of Li [24]. In the range of 10–15 GPa, the mixture of $\text{K}_2\text{CO}_3\text{-III}$ and $\text{K}_2\text{CO}_3\text{-IV}$ or another new phase, $\text{K}_2\text{CO}_3\text{-IIIb}$, is observed. $\text{K}_2\text{CO}_3\text{-IV}$ has low-temperature and high-temperature forms, $\alpha\text{-K}_2\text{CO}_3\text{-IV}$ and $\beta\text{-K}_2\text{CO}_3\text{-IV}$, respectively. The changes of diffraction pattern during α - to β phase transformation is illustrated in Figure S3. Comparison of diffraction patterns of phases III and IV was obtained in DAC and MA settings, see Figures S4 and S5.

The obtained phase diagrams according to MA and DAC-APS experiments are shown in Figure 7. The phase diagrams from these two experimental settings are consistent with each other. They are also consistent with available data on melting curves and high-pressure phase transitions of K_2CO_3 [24–26], suggesting one phase transition at 3 GPa and another-in the range of 13–25 GPa.

3.2.2 Indexing of Experimental Diffraction Patterns

According to theoretical predictions [31], $\gamma\text{-K}_2\text{CO}_3$ undergoes transition to $\text{K}_2\text{CO}_3\text{-P}\bar{1}$ at 12 GPa. $\text{K}_2\text{CO}_3\text{-P}\bar{1}$ is the structural analogue of $\text{Na}_2\text{CO}_3\text{-P}2_1/m$. We mentioned this structural similarity in our previous work [31]; within the present investigation we analyse the pseudosymmetry of $\text{K}_2\text{CO}_3\text{-P}\bar{1}$ and find out that atomic shifts less than 0.07 \AA increase the symmetry of the structure to $P2_1/m$. Below we will use $\text{K}_2\text{CO}_3\text{-P}2_1/m$ structure instead of $\text{K}_2\text{CO}_3\text{-P}\bar{1}$ for indexing of experimental diffraction patterns.

Most of the peaks of $\alpha\text{-K}_2\text{CO}_3\text{-IV}$ diffraction pattern can be satisfactorily indexed with $\text{K}_2\text{CO}_3\text{-P}2_1/m$ structure, except of several intense ones (Figure 8). Structural data of $\text{K}_2\text{CO}_3\text{-P}2_1/m$

used for indexing of experimental diffraction patterns are shown in Table S2. Based on the similarity of the experimental and theoretical diffraction patterns, phase IV can be considered as some structural analogue of K_2CO_3 - $P2_1/m$. In this case, unindexed peaks are explained by the structural difference of $P2_1/m$ and IV phases. However, they can be also explained by the presence of $P2_1/m$ phase in the mixture with the second phase with a similar structure. In this case, the changing of diffraction peak intensities observed in MA experiments (Figure S3) is due to the changing of the ratio of these two phases.

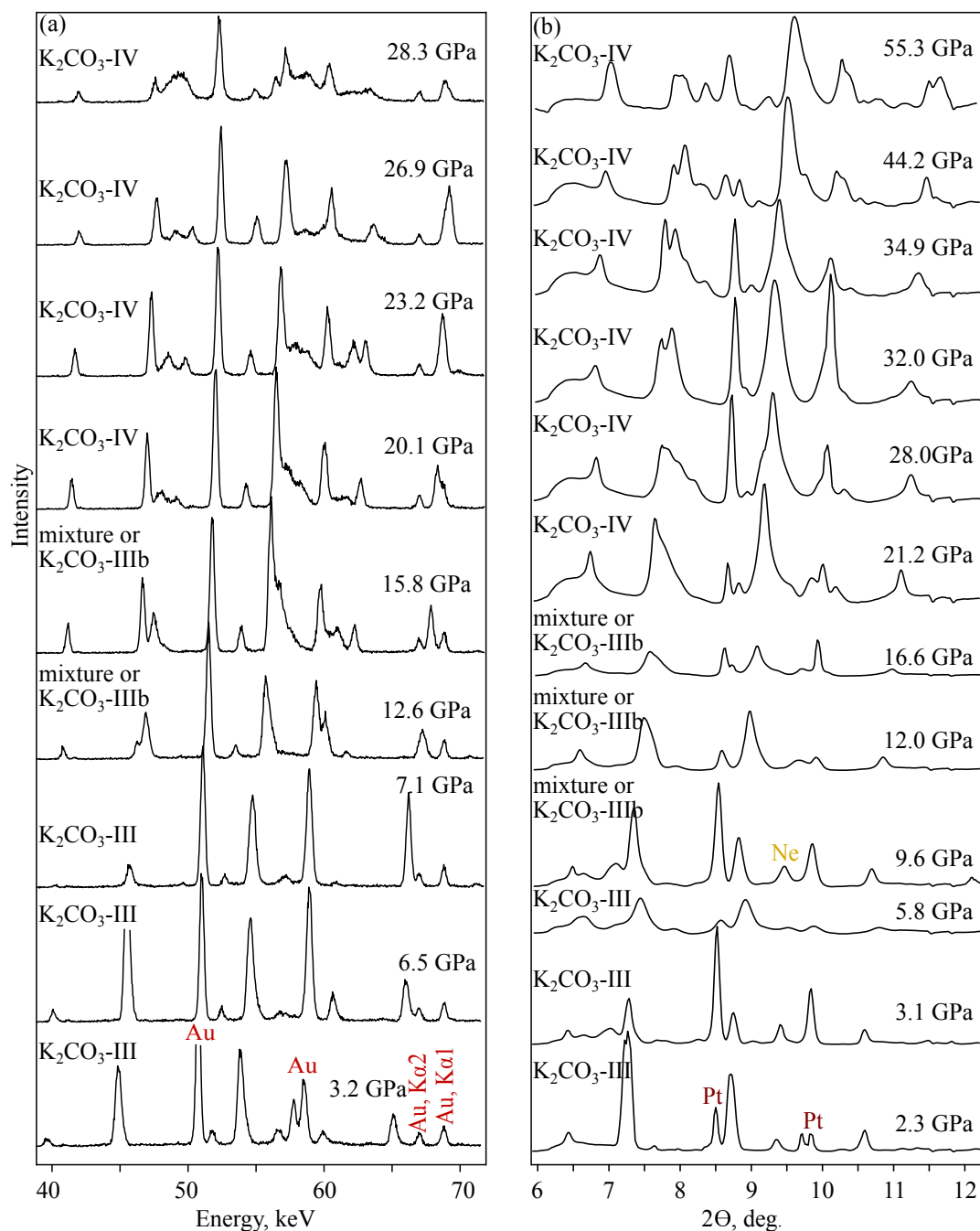


Figure 6. Diffraction patterns of K_2CO_3 collected in MA (a) and DAC-APS (b) experiments at room temperature.

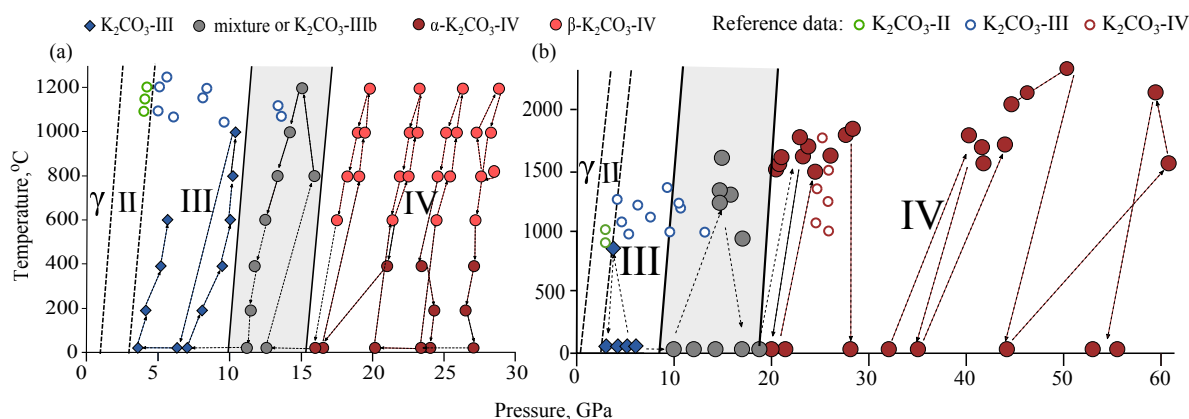


Figure 7. Phase diagrams of K_2CO_3 from MA (a) and DAC-APS (b) experiments. Empty circles reference the data of Li [24].

None of the high pressure diffraction patterns of K_2CO_3 can be indexed with $P6_3/mcm$ structure, observed for Na_2CO_3 and Li_2CO_3 [54]. Thus, stability field of $P6_3/mcm$ structure shrinks with increasing of cation radius. For Li_2CO_3 [54] it is observed in the range of 10–25 GPa, for Na_2CO_3 ; in the range of 12–26 GPa and for K_2CO_3 it is not observed at all.

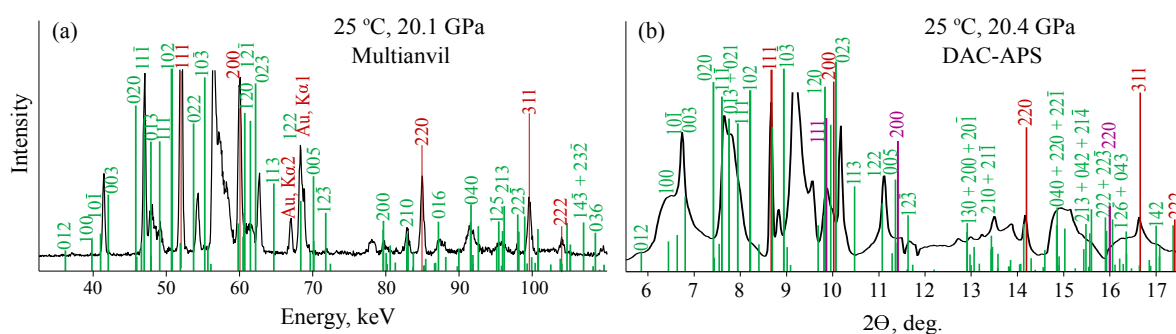


Figure 8. Indexing of diffraction patterns of α - K_2CO_3 -IV from MA (a) and DAC-APS (b) experiments with K_2CO_3 - $P2_1/m$ structure. The peaks of K_2CO_3 - $P2_1/m$ are shown in green, peaks of Au pressure marker in red and that of Ne in yellow.

3.2.3 The Effect of Water

To estimate the effect of water on the high-pressure transitions of K_2CO_3 we have performed two DAC experiments, (I) with loading in a glovebox and (II) with loading in the air. Silicone oil was used as the pressure transmitting medium in both cases. These experiments have been performed at SSTRC. DAC used in these experiments has a larger working chamber than in the experiments performed at APS and it is better suited for the studying of low-pressure phase transitions. All SSTRC experiments have been performed at room temperature.

In dry experiment (I), γ - K_2CO_3 is stable up to the maximum reached pressure of 6.8 GPa. The observed amorphization, starting from 3 GPa, is due to non-hydrostatic compression in silicon oil [55]. In wet experiment (II), the new phase or phases are observed above 3.1 GPa (Figure 9). The diffraction pattern of this phase is different from diffraction patterns of K_2CO_3 -III obtained in MA and DAC-APS experiments at nearly the same pressures (Figure S4).

The catalytic activity of K_2CO_3 in the transesterification reaction of fatty acid glycerides with alcohols, used for the production of biodiesel from food grade vegetable oils [56], was the motivation for us to perform the third (III) experiment with methanol as a pressure transmitting media. The loading has been done on the air to make experimental conditions similar to those in the production of bio-diesel. The result of this experiment is surprising. At the first pressure point, 0.5 GPa, we observed the diffraction pattern of the same phase, which was synthesised in experiment (II) at 3.1 GPa (Figure 9).

This phase (or phases) can be one of the hydrated form of K_2CO_3 , one of the K_2CO_3 high-pressure phases or a mixture of hydrate and high-pressure phase.

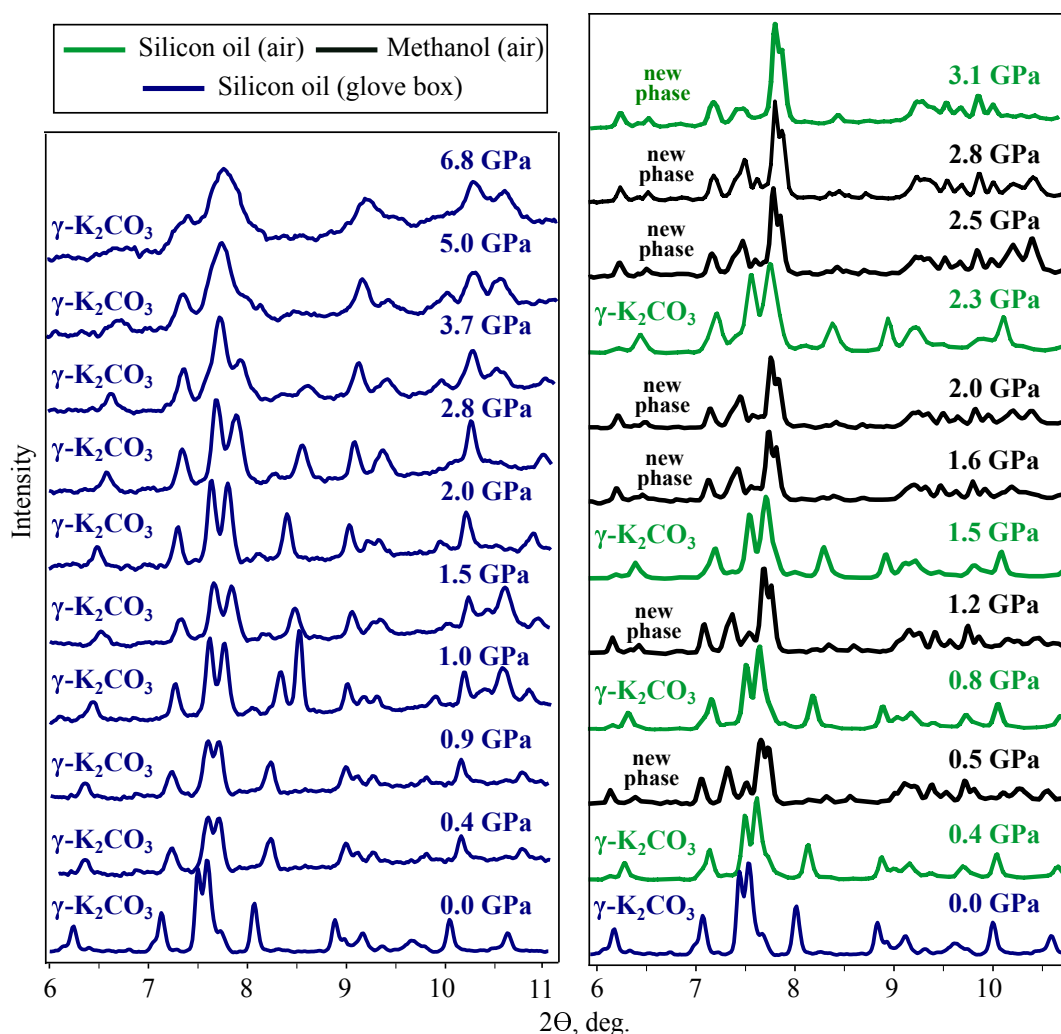


Figure 9. Diffraction patterns recorded in DAC-SSTRC experiments. Results of experiment (I) are shown in green, of experiment (II) in black and of experiment (III) in blue.

4. Theoretical P-T Diagrams and Stability of The Phases

Calculated phonon dispersion curves show dynamical instability of α - and β -phases for both Na_2CO_3 and K_2CO_3 . This is consistent with the unquenchable character of these phases ([57,58] and references therein). The average structure of γ - Na_2CO_3 is also unstable (Figure S6a). The last fact is not surprising. The real structure of γ -phase is incommensurately modulated, with amplitudes of modulations reaching 0.4 \AA [39]. The modulations likely stabilise the structure and the average structure without them became unstable. Other structures revealed in experiments, Na_2CO_3 - $P6_3/mcm$, Na_2CO_3 - $P2_1/m$, γ - K_2CO_3 and K_2CO_3 - $P2_1/m$, are dynamically stable (Figures S6 and S7).

The calculated values of unit cell volumes for γ - Na_2CO_3 and Na_2CO_3 - $P6_3/mcm$ closely reproduce experimental $V(P)$ dependence (Figure 10). As GGA pseudopotentials slightly overestimates volume, theoretical points lie higher than experimental ones. The fact that experimental points of γ - Na_2CO_3 at 8.6 and 9.6 GPa lie higher than theoretical ones is due to the uncertainty in experimental determination of unit cell volume of γ -phase at high pressures. Parameters of the Vinet equation of state [59] for γ - and $P6_3/mcm$ -phases determined by the theoretical points are the following:

$$\gamma\text{-Na}_2\text{CO}_3: E_{0,300} = -148.046 \text{ eV}, K_{0,300} = 37.56 \text{ GPa}, K'_{0,300} = 5.504, V_0 = 288.299 \text{ \AA}^3,$$

$$\text{Na}_2\text{CO}_3\text{-}P6_3/mcm: E_{0,300} = -73.773 \text{ eV}, K_{0,300} = 44.33 \text{ GPa}, K'_{0,300} = 5.73, V_0 = 137.505 \text{ \AA}^3.$$

The calculated P-T boundaries for $\gamma \leftrightarrow P6_3/mcm$ and $P6_3/mcm \leftrightarrow P2_1/m$ equilibria correctly reproduce experimental results on phase transitions of Na_2CO_3 (Figure 11a). According to calculations, both $P6_3/mcm$ and $P2_1/m$ structures are stable within all of the investigated temperature range, likely up to the melting temperatures. The upper stability boundary of $Pm\bar{m}n$ structure of Na_2CO_3 , revealed in our previous calculations [31], is restricted to nearly 0 °C (Figure 11). Due to sufficient structural difference between γ and $Pm\bar{m}n$ phases, the $\gamma \rightarrow Pm\bar{m}n$ transformation is hindered by the kinetic of the process.

The calculated stability field of $\text{K}_2\text{CO}_3\text{-}P2_1/m$ spreads from ~10 GPa to ~55 GPa. At higher pressure $P2_1/m$ structure transforms into $C2/c$ structure (Figure 11b). According to obtained experimental data, phase IV of K_2CO_3 was observed within the same P-T field. This is consistent with the assumption about structural similarity or even isostructurality of $P2_1/m$ and IV phases of K_2CO_3 .

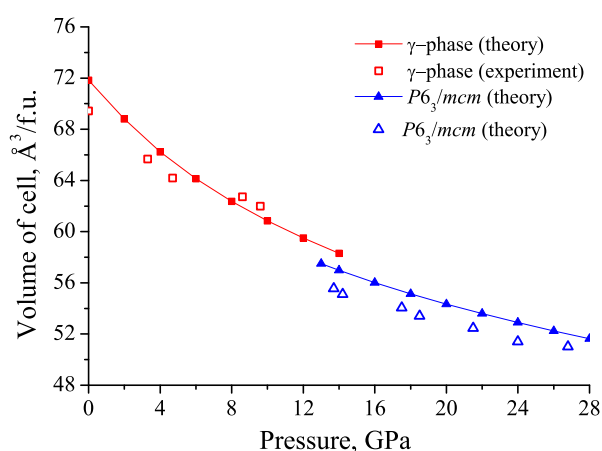


Figure 10. Theoretical and experimental pressure $V(P)$ dependencies for γ - and $P6_3/mcm$ phases of Na_2CO_3 . Solid red and blue lines correspond to the EOSs of γ and $P6_3/mcm$ phases determined by the theoretical points.

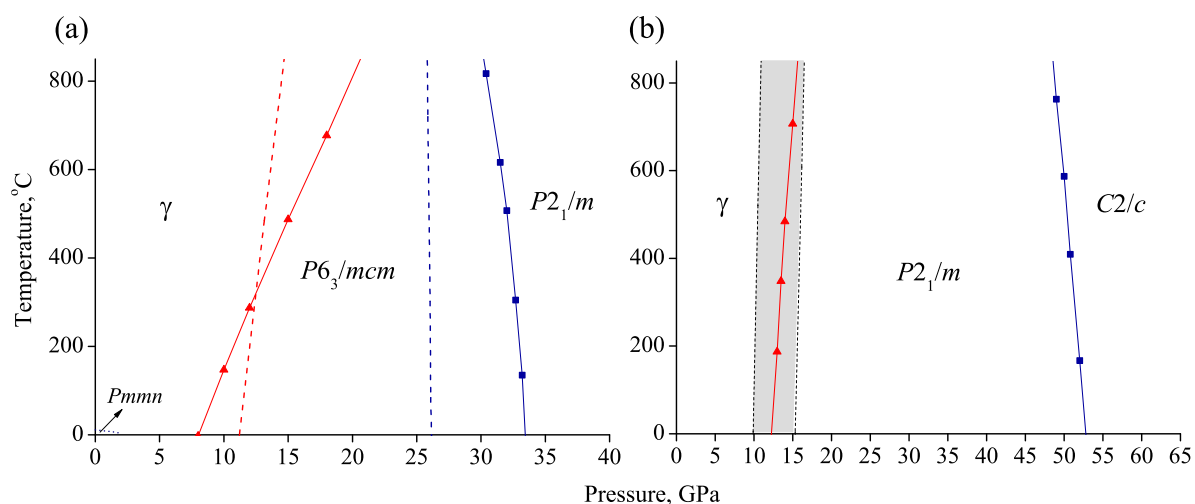


Figure 11. Theoretical P-T diagrams of Na_2CO_3 (a) and K_2CO_3 (b). Theoretical phase boundaries are shown in solid lines, experimental in dashed lines.

5. Discussion

For both K_2CO_3 and Na_2CO_3 , γ -phases are characterised by the same Ni_2In type of cation array and differ only in the tilt of CO_3 triangles [60]. Our results show quite a wide stability field of

γ - Na_2CO_3 and very narrow stability field of γ - K_2CO_3 (Figure 12). This can be explained by the sufficient difference in the size of Na^+ and K^+ ions. Na^+ ion fits better to Ni_2In type than the big K^+ [61]. As a result, γ - K_2CO_3 readily transforms to another structural type (phases II, III and IV) at relatively small compression. Li^+ is, in turn, too small and does not adopt Ni_2In type at all, its γ form is of CaF_2 type [60].

Comparison of high-pressure phase transitions of alkaline carbonates, Li_2CO_3 , Na_2CO_3 and K_2CO_3 is presented on Figure 12. It shows that there are two main high-pressure structures of alkaline carbonates, $P6_3/mcm$ and $P2_1/m$. $P2_1/m$ structure is characterised by the higher coordination numbers, cations of alkaline metal in this structure are surrounded by seven or eight oxygens, disposed in the vertices of the deformed cube or two-capped trigonal prism, while in $P6_3/mcm$ structure the coordination of alkaline metal by oxygen equals six and the coordination polyhedron is octahedron (Figure S8). As a result, the stability fields of $P6_3/mcm$ -phases shrink with an increase in cation radius from Li^+ to K^+ , while stability fields of $P2_1/m$ structures, assuming K_2CO_3 -IV as the analogue of K_2CO_3 - $P2_1/m$, expands.

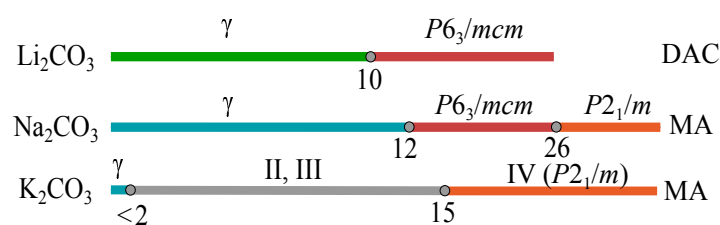


Figure 12. Scheme, summarising experimental data on high-pressure phase transitions of Li_2CO_3 [54], Na_2CO_3 (this work) and K_2CO_3 (this work). Numbers show pressures of phase transitions in GPa. Similar crystal structures are shown in the same colours.

Supplementary Materials: The following are available online at <http://www.mdpi.com/2075-163X/9/10/599/s1>, Figure S1: Experimental diffraction patterns at 13.7 GPa (a) and at 27.9 GPa (b) with theoretical peaks of Na_2CO_3 - $P6_3/mcm$ (a) and Na_2CO_3 - $P2_1/m$ (b) structures. Peaks of the structure optimised with LDA are shown with thin blue lines, with GGA—with turquoise thin lines, and of the averaged structure—with thick violet lines; Figure S2: Rietveld refinement of Na_2CO_3 - $P6_3/mcm$ structure with MA diffraction pattern recorded at 13.7 GPa and 27 °C, R-factor = 27%; Figure S3: Changes of diffraction pattern on heating at pressures 26.9–28.8 GPa according to MA setting; Figure S4: Diffraction patterns in DAC-SSTRC (a), DAC-APS (b), and multianvil (c) settings at 2.3–3.6 GPa. Grey bands are shown for the convenience of visual comparison; Figure S5: Diffraction patterns of K_2CO_3 -IV recorded in DAC-APS (a) and multianvil (b) settings; Figure S6: Phonon dispersion curves of Na_2CO_3 phases, $Pm\bar{m}n$ at 0 GPa (a), γ at 12 GPa (b), and $P6_3/mcm$ at 24 GPa (c) and $P2_1/m$ at 36 GPa (d); Figure S7: Phonon dispersion curves of K_2CO_3 phases, β at 0 GPa (a), γ at 1 GPa (b), $P2_1/m$ at 36 GPa (c) and $C2/c$ at 60 GPa (d); Figure S8: Na-O polyhedrons in $P6_3/mcm$ (a) and $P2_1/m$ (b) crystal structures of Na_2CO_3 . Table S1: Unit cell parameters of γ - Na_2CO_3 from DAC-APS experiments; Table S2: Structural data of K_2CO_3 - $C2/m$ used for indexing of experimental diffraction pattern (according to DFT calculations, without refinement).

Author Contributions: Conceptualization, P.N.G., A.S. and K.D.L.; methodology, P.N.G., A.S., S.S.L., K.D.L., A.Y.L., A.F.G., and I.S.S.; software, S.V.R.; validation, A.B. and S.V.R.; formal analysis, A.B., S.V.R., D.S., N.S., and A.Y.L.; investigation, P.N.G., A.B., D.S., and N.S.; resources, V.B.P., and Y.H.; writing—original draft preparation, P.N.G.; writing—review and editing, P.N.G. and K.D.L.; visualization, P.N.G. and A.B.; supervision, K.D.L., and A.F.G.

Funding: This research was funded by Russian Science Foundation (project No 14-17-00609-P). SSL was supported by Helmholtz Young Investigators Group CLEAR (VH-NG-1325).

Acknowledgments: We thank the Information Technology Centre of Novosibirsk State University for providing access to the cluster computational resources. A.F.G. and K.D.L. acknowledge support from Alfred P. Sloan Foundation via the Deep Carbon Observatory program.

Conflicts of Interest: The authors declare no conflict of interest.

References

- Zubkova, N.; Pushcharovsky, D. Y.; Ivaldi, G.; Ferraris, G.; Pekov, I.; Chukanov, N. Crystal structure of natrite, γ - Na_2CO_3 . *Neues Jahrb. FÜR-Mineral. Monatshefte* **2002**, *2002*, 85–96.

2. Gittins, J.; McKie, D. Alkalic carbonatite magmas: Oldoinyo Lengai and its wider applicability. *Lithos* **1980**, *13*, 213–215.
3. Zaitsev, A.; Keller, J.; Spratt, J.; Jeffries, T.; Sharygin, V. Chemical composition of nyerereite and gregoryite from natrocarbonatites of Oldoinyo Lengai volcano, Tanzania. *Geol. Ore Depos.* **2009**, *51*, 608–616.
4. Bolotina, N.B.; Gavryushkin, P.N.; Korsakov, A.V.; Rashchenko, S.V.; Seryotkin, Y.V.; Golovin, A.V.; Moine, B.N.; Zaitsev, A.N.; Litasov, K.D. Incommensurately modulated twin structure of nyerereite $\text{Na}_{1.64}\text{K}_{0.36}\text{Ca}(\text{CO}_3)_2$. *Struct. Sci. Cryst. Eng. Mater.* **2017**, *73*, 276–284.
5. Gavryushkin, P. N.; Thomas, V. G.; Bolotina, N. B.; Bakakin, V. V.; Golovin, A. V.; Seryotkin, Y. V.; Fursenko, D. A.; Litasov, K. D. Hydrothermal synthesis and structure solution of $\text{Na}_2\text{Ca}(\text{CO}_3)_2$: “synthetic analogue” of mineral nyerereite. *Cryst. Growth Des.* **2016**, *16*, 1893–1902.
6. McKie, D.; Frankis, E. Nyerereite: A new volcanic carbonate mineral from Oldoinyo Lengai, Tanzania. *Z. Kristallogr. Cryst. Mater.* **1977**, *145*, 73–95.
7. Golovin, A. V.; Sharygin, I. S.; Korsakov, A. V. Origin of alkaline carbonates in kimberlites of the siberian craton: Evidence from melt inclusions in mantle olivine of the Udachnaya-East pipe. *Chem. Geol.* **2017**, *455*, 357–375.
8. Egorov, K.; Ushchapovskaia, Z.; Kashaev, A.; Bogdanov, G.; Sizykh, I. I. Zemkorite—a new carbonate from yakutian kimberlites. *Akad. Nauk. SSSR Dokl.* **1988**, *301*, 188–193.
9. Dickens, B.; Hyman, A.; Brown, W. Crystal structure of $\text{Ca}_2\text{Na}_2(\text{CO}_3)_3$ (shortite). *J. Res. Natl. Bur. Stand. Sec. A Phys. Chem.* **1971**, *75*, 129–140.
10. Pabst, A. The crystallography structure of eitelite, $\text{Na}_2\text{Mg}(\text{CO}_3)_2$. *Am. Mineral.* **1973**, *58*, 211–217.
11. Pertlik, F. Structural investigations of synthetic fairchildite, $\text{K}_2\text{Ca}(\text{CO}_3)_2$. *Z. Kristallogr.* **1981**, *157*, 199–205.
12. Hesse, K.-F.; Simons, B. Crystal structure of synthetic $\text{K}_2\text{Mg}(\text{CO}_3)_2$. *Z. Kristallogr. Cryst. Mater.* **1982**, *161*, 289–292.
13. Shatskiy, A.; Rashchenko, S.V.; Ohtani, E.; Litasov, K.D.; Khlestov, M.V.; Borzdov, Y.M.; Kupriyanov, I.N.; Sharygin, I.S.; Palyanov, Y.N. The system $\text{Na}_2\text{CO}_3\text{-FeCO}_3$ at 6 GPa and its relation to the system $\text{Na}_2\text{CO}_3\text{-FeCO}_3\text{-MgCO}_3$. *Am. Mineral.* **2015**, *100*, 130–137.
14. Gavryushkin, P. N.; Bakakin, V. V.; Bolotina, N. B.; Shatskiy, A. F.; Seryotkin, Y. V.; Litasov, K. D. Synthesis and crystal structure of new carbonate $\text{Ca}_3\text{Na}_2(\text{CO}_3)_4$ homeotypic with orthoborates $\text{M}_3\text{Ln}_2(\text{BO}_3)_4$ (M=Ca, Sr and Ba). *Cryst. Growth Des.* **2014**, *14*, 4610–4616.
15. Shatskiy, A.; Gavryushkin, P. N.; Litasov, K. D.; Koroleva, O. N.; Kupriyanov, I. N.; Borzdov, Y. M.; Sharygin, I. S.; Funakoshi, K.; Palyanov, Y. N.; Ohtani, E. Na-Ca carbonates synthesized under upper-mantle conditions: Raman spectroscopic and X-ray diffraction studies. *Eur. J. Mineral.* **2015**, *27*, 175–184.
16. Shatskiy, A.; Sharygin, I. S.; Litasov, K. D.; Borzdov, Y. M.; Palyanov, Y. N.; Ohtani, E. New experimental data on phase relations for the system $\text{Na}_2\text{CO}_3\text{-CaCO}_3$ at 6 GPa and 900–1400 °C. *Am. Mineral.* **2013**, *98*, 2164–2171.
17. Rashchenko, S.V.; Bakakin, V.V.; Shatskiy, A.F.; Gavryushkin, P.N.; Seryotkin, Y.V.; Litasov, K.D. Noncentrosymmetric $\text{Na}_2\text{Ca}_4(\text{CO}_3)_5$ carbonate of “ $\text{M}_1\text{M}_2\text{XY}_3\text{Z}$ ” structural type and affinity between borate and carbonate structures for design of new optical materials. *Cryst. Growth Des.* **2017**, *17*, 6079–6084.
18. Song, Y.; Luo, M.; Zhao, D.; Peng, G.; Lin, C.; Ye, N. Explorations of new UV nonlinear optical materials in the $\text{Na}_2\text{CO}_3\text{-CaCO}_3$ system. *J. Mater. Chem.* **2017**, *5*, 8758–8764.
19. Podborodnikov, I.V.; Shatskiy, A.; Arefiev, A.V.; Rashchenko, S.V.; Chanyshv, A.D.; Litasov, K.D. The system $\text{Na}_2\text{CO}_3\text{-CaCO}_3$ at 3 GPa. *Phys. Chem. Miner.* **2018**, *45*, 773–1787.
20. Rashchenko, S. V.; Shatskiy, A. F.; Arefiev, A. V.; Seryotkin, Y. V.; Litasov, K. D. $\text{Na}_4\text{Ca}(\text{CO}_3)_3$: A novel carbonate analog of borate optical materials. *CrystEngComm* **2018**, *20*, 6358–6358.
21. Kaminsky, F. V.; Wirth, R.; Schreiber, A. Carbonatitic inclusions in deep mantle diamond from Juina, Brazil: new minerals in the carbonate-halide association. *Can. Mineral.* **2013**, *51*, 669–688.
22. Kaminsky, F.; Matzel, J.; Jacobsen, B.; Hutcheon, I.; Wirth, R. Isotopic fractionation of oxygen and carbon in decomposed lower-mantle inclusions in diamond. *Mineral. Petrol.* **2016**, *110*, 379–385.
23. Li, Z.; Li, J.; Lange, R.; Liu, J.; Militzer, B. Determination of calcium carbonate and sodium carbonate melting curves up to Earth’s transition zone pressures with implications for the deep carbon cycle. *Earth Planet. Sci. Lett.* **2017**, *457*, 395–402.
24. Li, Z. Melting and Structural Transformations of Carbonates and Hydrous Phases in Earth’s Mantle. Ph.D. Thesis, University of Michigan, Ann Arbor, MI, USA, 2015.

25. Wang, M.; Liu, Q.; Inoue, T.; Li, B.; Pottish, S.; Wood, J.; Yang, C.; Tao, R. The K_2CO_3 fusion curve revisited: New experiments at pressures up to 12 GPa. *J. Mineral. Petrol. Sci.* **2016**, *111*, 241–251.
26. Liu, Q.; Tenner, T. J.; Lange, R. A. Do carbonate liquids become denser than silicate liquids at pressure? Constraints from the fusion curve of K_2CO_3 to 3.2 GPa. *Contrib. Mineral. Petrol.* **2007**, *153*, 55–66.
27. Klement, W., Jr.; Cohen, L.H. Solid-solid and solid-liquid transitions in K_2CO_3 , Na_2CO_3 and Li_2CO_3 : Investigations to ≥ 5 kbar by differential thermal analysis; thermodynamics and structural correlations. *Berichte Bunsenges. FÜR Phys. Chem.* **1975**, *79*, 327–334.
28. Shatskiy, A.; Sharygin, I. S.; Gavryushkin, P. N.; Litasov, K. D.; Borzdov, Y. M.; Shcherbakova, A. V.; Higo, Y.; Funakoshi, K.-i.; Palyanov, Y. N.; Ohtani, E. The system K_2CO_3 - $MgCO_3$ at 6 GPa and 900–1450 °C. *Am. Mineral.* **2013**, *98*, 1593–1603.
29. Arefiev, A.V.; Shatskiy, A.; Podborodnikov, I.V.; Rashchenko, S.V.; Chanyshv, A.D.; Litasov, K.D. The system K_2CO_3 - $CaCO_3$ at 3 GPa: Link between phase relations and variety of K-Ca double carbonates at ≤ 0.1 and 6 GPa. *Phys. Chem. Miner.* **2018**, 1–16. doi:10.2138/am.2013.4436 .
30. Čančarevič, Ž.; Schön, J.; Jansen, M. Alkali metal carbonates at high pressure. *Z. Anorg. Allg. Chem.* **2006**, *632*, 1437–1448.
31. Gavryushkin, P. N.; Behtenova, A.; Popov, Z. I.; Bakakin, V. V.; Likhacheva, A. Y.; Litasov, K. D.; Gavryushkin, A. Toward analysis of structural changes common for alkaline carbonates and binary compounds: Prediction of high-pressure structures of Li_2CO_3 , Na_2CO_3 and K_2CO_3 . *Cryst. Growth Des.* **2016**, *16*, 5612–5617.
32. Katsura, T.; Funakoshi, K.-i.; Kubo, A.; Nishiyama, N.; Tange, Y.; Sueda, Y.-i.; Kubo, T.; Utsumi, W. A large-volume high-pressure and high-temperature apparatus for in situ X-ray observation, 'SPEED-Mk. II'. *Phys. Earth Planet. Inter.* **2004**, *143*, 497–506.
33. Sokolova, T.S.; Dorogokupets, P.I.; Dymshits, A.M.; Danilov, B.S.; Litasov, K.D. Microsoft excel spreadsheets for calculation of P-V-T relations and thermodynamic properties from equations of state of MgO, diamond and nine metals as pressure markers in high-pressure and high-temperature experiments. *Comput. Geosci.* **2016**, *94*, 162–169.
34. Prakupenka, V.; Kubo, A.; Kuznetsov, A.; Laskin, A.; Shkurikhin, O.; Dera, P.; Rivers, M.; Sutton, S. Advanced flat top laser heating system for high pressure research at gsecars: Application to the melting behavior of germanium. *High Press. Res.* **2008**, *28*, 225–235.
35. Gavryushkin, P.; Rashchenko, S.; Shatskiy, A.; Litasov, K.; Ancharov, A. Compressibility and phase transitions of potassium carbonate at pressures below 30 kbar. *J. Struct. Chem.* **2016**, *57*, 1485–1488.
36. Piminov, P.; Baranov, G.; Bogomyagkov, A.; Berkaev, D.; Borin, V.; Dorokhov, V.; Karnae, S.; Kiselev, V.; Levichev, E.; Meshkov, O.; et al. Synchrotron radiation research and application at VEPP-4. *Phys. Procedia* **2016**, *84*, 19–26.
37. Hammersley, A.; Svensson, S.; Hanfland, M.; Fitch, A.; Hausermann, D. Two-dimensional detector software: From real detector to idealised image or two-theta scan. *Int. J. High Press. Res.* **1996**, *14*, 235–248.
38. Rashchenko, S. V.; Kurnosov, A.; Dubrovinsky, L.; Litasov, K. D. Revised calibration of the sm: SrB_4O_7 pressure sensor using the sm-doped yttrium-aluminum garnet primary pressure scale. *J. Appl. Phys.* **2015**, *117*, 145902.
39. Dušek, M.; Chapuis, G.; Meyer, M.; Petricek, V. Sodium carbonate revisited. *Acta Crystallogr. Sect. B Struct. Sci* **2003**, *59*, 337–352.
40. Blöchl, P. E. Projector augmented-wave method. *Phys. Rev. B* **1994**, *50*, 17953.
41. Kresse, G.; Furthmüller, J. Efficient iterative schemes for ab initio total-energy calculations using a plane-wave basis set. *Phys. Rev. B* **1996**, *54*, 11169.
42. Kresse, G.; Furthmüller, J. Efficiency of ab-initio total energy calculations for metals and semiconductors using a plane-wave basis set. *Comput. Mater. Sci.* **1996**, *6*, 15–50.
43. Kresse, G.; Joubert, D. From ultrasoft pseudopotentials to the projector augmented-wave method. *Phys. Rev. B* **1999**, *59*, 1758.
44. Perdew, J. P.; Burke, K.; Ernzerhof, M. Generalized gradient approximation made simple. *Phys. Rev. Lett.* **1996**, *77*, 3865.
45. Stokes, H. T.; Hatch, D. M. FINDSYM: Program for identifying the space-group symmetry of a crystal. *J. Appl. Crystallogr.* **2005**, *38*, 237–238.
46. Momma, K.; Izumi, F. VESTA 3 for three-dimensional visualization of crystal, volumetric and morphology data. *J. Appl. Crystallogr.* **2011**, *44*, 1272–1276.

47. Togo, A.; Oba, F.; Tanaka, I. First-principles calculations of the ferroelastic transition between rutile-type and CaCl_2 -type SiO_2 at high pressures. *Phys. Rev. B* **2008**, *78*, 134106.
48. Seto, Y. Development of a software suite on X-ray diffraction experiments. *Rev. High Press. Sci. Technol.* **2010**, *20*, 269–276.
49. Toby, B. H.; Von Dreele, R. B. Gsas-II: The genesis of a modern open-source all purpose crystallography software package. *J. Appl. Crystallogr.* **2013**, *46*, 544–549.
50. Shatskiy, A.; Gavryushkin, P.N.; Sharygin, I.S.; Litasov, K.D.; Kupriyanov, I.N.; Higo, Y.; Borzdov, Y.M.; Funakoshi, K.; Palyanov, Y.N.; Ohtani, E. Melting and subsolidus phase relations in the system $\text{Na}_2\text{CO}_3\text{-MgCO}_3 \pm \text{H}_2\text{O}$ at 6 GPa and the stability of $\text{Na}_2\text{Mg}(\text{CO}_3)_2$ in the upper mantle. *Am. Mineral.* **2013**, *98*, 2172–2182.
51. Merlini, M.; Hanfland, M.; Crichton, W. CaCO_3 -III and CaCO_3 -VI, high-pressure polymorphs of calcite: Possible host structures for carbon in the Earth's mantle. *Earth Planet. Sci. Lett.* **2012**, *333*, 265–271.
52. Gavryushkin, P.N.; Martirosyan, N.S.; Inerbaev, T.M.; Popov, Z.I.; Rashchenko, S.V.; Likhacheva, A.Y.; Lobanov, S.S.; Goncharov, A.F.; Prakapenka, V.B.; Litasov, K.D. Aragonite-II and CaCO_3 -VII: New high-pressure, high-temperature polymorphs of CaCO_3 . *Cryst. Growth Des.* **2017**, *17*, 6291–6296.
53. Litasov, K. D.; Shatskiy, A.; Gavryushkin, P. N.; Bekhtenova, A. E.; Dorogokupets, P. I.; Danilov, B. S.; Higo, Y.; Akilbekov, A. T.; Inerbaev, T. M. PVT equation of state of CaCO_3 aragonite to 29 GPa and 1673 K: In situ x-ray diffraction study. *Phys. Earth Planet. Inter.* **2017**, *265*, 82–91.
54. Grzechnik, A.; Bouvier, P.; Farina, L. High-pressure structure of Li_2CO_3 . *J. Solid State Chem.* **2003**, *173*, 13–19.
55. Klotz, S.; Chervin, J.; Munsch, P.; Le Marchand, G. Hydrostatic limits of 11 pressure transmitting media. *J. Phys. Appl. Phys.* **2009**, *42*, 075413.
56. Malins, K. The potential of K_3PO_4 , K_2CO_3 , Na_3PO_4 and Na_2CO_3 as reusable alkaline catalysts for practical application in biodiesel production. *Fuel Process. Technol.* **2018**, *179*, 302–312.
57. Maciel, A.; Ryan, J.; Walker, P. Structural phase transitions in K_2CO_3 (raman scattering study). *J. Phys. Solid State Phys.* **1981**, *14*, 1611.
58. Swainson, I.; Dove, M.; Harris, M. J. Neutron powder diffraction study of the ferroelastic phase transition and lattice melting in sodium carbonate, Na_2CO_3 . *J. Phys. Condens. Matter* **1995**, *7*, 4395.
59. Vinet, P.; Ferrante, J.; Rose, J.; Smith, J. Compressibility of solids. *J. Geophys. Res. Solid Earth* **1987**, *92*, 9319–9325.
60. Blatov, V. A. Crystal structures of inorganic oxoacid salts perceived as cation arrays: A periodic-graph approach. In *Inorganic 3D Structures*; Springer: Berlin/Heidelberg, Germany, 2011; pp. 31–66.
61. Shannon, R. D.; Prewitt, C.T. Revised values of effective ionic radii. *Acta Crystallogr. Sect. Struct. Crystallogr. Cryst. Chem.* **1970**, *26*, 1046–1048.



© 2019 by the authors. Licensee MDPI, Basel, Switzerland. This article is an open access article distributed under the terms and conditions of the Creative Commons Attribution (CC BY) license (<http://creativecommons.org/licenses/by/4.0/>).